OFDM-Based Intrinsically Safe Power and Signal Synchronous Transmission for CC-PT-Controlled Buck Converters

Yang Leng, Dongsheng Yu, *Member, IEEE*, Kunfeng Han, Samson Shenglong Yu, *Member, IEEE*, and Yihua Hu, *Senior Member, IEEE*

***Abstract*—Intrinsically safe power converters have been highly demanded in many harsh industrial environments, such as gas stations, chemical plants, and mine tunnels, to realize accurate voltage or current regulations with minimum safety risks. Communication among different devices is the key to realizing important operations, such as coordinated control, fault detection, and state update, for intrinsically safe converters. In this article, a capacitor current pulse train (CC-PT) control strategy is designed to increase the dynamic response of dc–dc converter with intrinsic operational safety. An orthogonal frequency-division multiplexing (OFDM) based power and signal synchronous transmission (PSST) method is then proposed. The mathematical models of signal modulation are established, and the intrinsic safety region is drawn in the *L–C* parameters plane, considering the requirements of electric performance, the inductor disconnection discharging, and output short-circuit tests. Simulations and prototype experiments are conducted and presented to verify the feasibility of the OFDM-based PSST in the CC-PT-controlled buck converter with intrinsically safe parameters.**

***Index Terms*—Capacitor current pulses train control, dc power supply system, intrinsically safe converter, orthogonal frequency-division multiplexing (OFDM), power and signal synchronous transmission (PSST).**

I. Introduction

SINCE the rapid popularization of intelligent electrical devices, power converters with fast response speed, high safety, and reliable communication have been highly desired in many industrial applications [1]–[3]. With regards to flammable and explosive environments, such as gas stations and chemical plants, power converters with intrinsic safety are utilized for providing the required voltage or current for different electrical devices [4], [5]. Limiting spark energy is vital requirement for electronics devices to operate in harsh environments where intrinsically safe converters are employed. Intrinsically safe converters require very small ripple amplitude to limit accidentally released spark energy, and fast response is needed for timely monitoring and alerting abnormal operation conditions in harsh environments.

Thus far, the pulsewidth modulation (PWM) and pulse frequency modulation (PFM) methods have been widely used for regulating dc–dc power converters [6]–[8]. Compared with the PWM and PFM strategies, the pulse train (PT) control method possesses the advantages of high response speed, simple structure, strong robustness, no control error compensator, and low cost, which is suitable for applications in harsh environments where timely alerting and high reliability are essential [9], [10]. However, after introducing PT control method to dc–dc converters in continuous conduction mode (CCM), low-frequency voltage oscillations (LFVOs) can be detected with unexpected high amplitudes. Hence, many LFVO suppression methods have been proposed to achieve fast response speed and steady output voltage of PT-controlled power converters [11], [12]. In [13], a capacitor-current-based PT control method is introduced to parallel-connected buck converters with current-sharing capability for achieving fast response speed. In [14], a peak capacitor-current-based PT control strategy is applied to buck converters for eliminating its fast-scale and low-frequency oscillations. In [15], a sliding valley current mode PT control strategy is proposed to minimize the controller cost and stabilize output voltage. It is reasonable to ponder that the response speed of intrinsically safe power converters can also be improved by integrating the PT control method.

In many cases, power converters need to configure communication functions to enable the operations of state update and fault detection, especially for power supplies with geographically distributed converters [16], [17]. Power and signal synchronous transmission (PSST) has been applied to power grid and dc–dc power converters thanks to its advantages of no requirement of extra communication line in hardware, signals can be transmitted together with power on well-established power lines [18]. In [19], PSST strategies are proposed and discussed by synchronously regulating output power and voltage ripples to transmit signals together with power conversion, where it is claimed as "talkative power," and the PSST strategies are

Manuscript received December 9, 2021; revised February 24, 2022; accepted March 24, 2022. Date of publication April 1, 2022; date of current version May 23, 2022. This work was supported by the National Natural Science Foundation of China under Grant 51977208. Recommended for publication by Associate Editor F. D. Freijedo. *(Corresponding authors: Dongsheng Yu; Yihua Hu.)*

Yang Leng, Dongsheng Yu, Kunfeng Han, and Yihua Hu are with the School of Electrical Engineering, China University of Mining and Technology, Xuzhou 221116, China (e-mail: lengyangandy@163.com; dongsiee@163.com; hankunfeng1995@163.com; yihua.hu@york.ac.uk).

Samson Shenglong Yu is with the School of Engineering, Deakin University, Melbourne, VIC 3125, Australia (e-mail: samson.yu@deakin.edu.au).

Color versions of one or more figures in this article are available at https://doi.org/10.1109/TPEL.2022.3164240.

Digital Object Identifier 10.1109/TPEL.2022.3164240

experimentally tested in practical dc–dc power converter systems. To facilitate the realization of internet of things and reduce supply cost, a power/signal dual modulation method containing PWM/FSK and PWM/PSK is proposed in [20] to realize PSST.

With regards to PSST among dc–dc power converters, the signal carriers are normally induced by tuning the switching frequency, duty cycle, or phase of PWM driving signals [21]–[23]. Nevertheless, signal transmission speed is unavoidably limited by the power switching frequency, and the same frequency harmonics from other interconnected dc converters could affect the demodulation accuracy. To solve this issue, the orthogonal frequency-division multiplexing (OFDM) method is applied to increase communication speed of PSST, because OFDM can realize parallel data transmission and antimultipath attenuation [24]. Also, the frequency of OFDM subcarriers can be flexibly selected for detouring the interference from the congested frequency band of dc networks. As has been experimentally proven, by incorporating OFDM strategy into PT-controlled dc–dc power converters with PSST configuration, the communication speed and reliability have been improved [25].

The intrinsic safety of power converter is mainly decided by the amount of energy stored in its inductors and capacitors, and electric sparks can be detected when this energy is suddenly released. As voltage ripples on the dc bus of power converters are regulated to carry information, the energy stored in their inductor and capacitor is altered and the intrinsic safety is hence unavoidably deteriorated. There is possibility that the voltage ripples regulated for carrying signals could cause re-emergence of LFVO to PT-controlled power converters and, hence, increase the energy variation inside inductor. Therefore, electric sparks can be produced and then increase the risk of igniting flammable gas when the inductor is disconnected or the output capacitor is short-circuited [26]–[28]. Hence, it is of great significance to redesign the intrinsically safe parameters for the power converters to be suitably configured for the PSST strategy.

To the best of our knowledge, neither the OFDM-based PSST strategy nor the capacitor current pulse train (CC-PT) control method has been utilized for designing intrinsically safe dc–dc converters in the literature. Therefore, the research work presented in this article is a new attempt to design intrinsically safe power converters with fast response speed and reliable communication. Signal transmission and intrinsic safety are two significant goals for designing the dc–dc converter in this study. To achieve intrinsic safety, the inductance and capacitance of a converter shall be carefully designed to restrict their inside stored energy to avoid dangerous discharging sparks. Meanwhile, the implementation of the PSST requires extra regulation of output voltage ripples to achieve signal transmission. Making a balanced tradeoff between these two requirements is the main concern of this article. The main challenges of utilizing these techniques include the mathematical modeling of the PT-controlled dc–dc converters system, intrinsically safe parameters design for converters with PSST, and the OFDM communication with a limited switching frequency.

In Section II, the traditional signal modulation mechanisms in a PT-controlled buck converter are briefly presented. The CC-PT/OFDM method for buck converter is discussed and modeled in Section III. In Section IV, considering the inductor disconnection discharging and the output short-circuit test requirements, the intrinsically safe parameters for the CC-PT-controlled buck converters are designed. In Section V, simulations and prototype experiments are carried out to validate the feasibility of the OFDM-based PSST in the CC-PT-controlled buck converter with intrinsic safety. Finally, Section VI concludes this article.

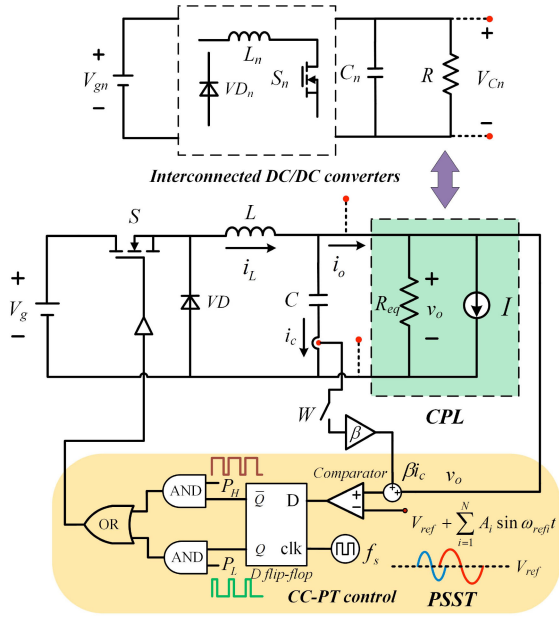

Fig. 1. PSST in the PT-controlled dc–dc converters system.

II. Signal Modulation in PT-Controlled Buck Converters

Since communication needs to be configured among numerous converters in a power supply system, a constant power load (CPL) is considered in this scheme as other converters connected with the primary converter in different types can be considered equivalent to a CPL [29]. Fig. 1 is the schematic of the PSST approach in a PT-controlled dc–dc converters system, where the interconnected converters are modeled as a CPL. W is the switch for the capacitor current feedback loop to mitigate the LFVO. $R_{\rm eq}$ and I are the equivalent resistance and current source, respectively. V_{Cn} is the average output voltage of load converter, and R is the load resistance. In the voltage comparison module, when the output voltage is higher than the reference voltage, low-power pulse P_L is selected, and when the output voltage is lower than the reference voltage, high-power pulse P_H is selected to regulate the output voltage. The clock for driving the D flip-flop is synchronized by the rising edges of P_H and P_L. Here, f_s is the switching frequency. To achieve PSST for dc–dc converters, the data and carriers are superimposed on the reference voltage to regulate the proportion of high- and low-power pulses.

Define that $v_{\rm o}$ is the output voltage, i_L is the inductor current, $V_{\rm o}$ is the average value of $v_{\rm o}$, V_g is the input voltage, I_o is the average value of the output current, and I is the equivalent current

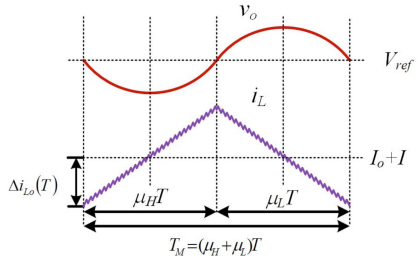

Fig. 2. Waveforms of output voltage v_o and inductor current i_L of the PT-controlled CCM converter.

of the CPL. The output power is defined as P. We have

$$P = \frac{V_{Cn}^2}{R} = v_o I. \tag{1}$$

For the PT-controlled CCM buck converter with CPL, the variations of output voltage and inductor current in the nth switching cycle are, respectively, expressed as

$$\begin{cases} \Delta v_o\,(nT) = \frac{T^2}{2LC}\left[(V_g D\,(2-D) - v_o\,(nT))\right] \\ \qquad\qquad + \frac{T}{C}[i_L\,(nT) - I_o - \frac{V_{Cn}^2}{R v_o(nT)}] \\ \Delta i_L\,(nT) = \frac{T}{L} V_g D - \frac{T}{L} V_o \end{cases} \tag{2}$$

where T is the switching period, and D is the duty cycle.

As shown in Fig. 2, when inductor current $i_L < I_o + I$, output voltage v_o decreases, and when $i_L > I_o + I$, v_o increases. $V_{\rm ref}$ is the reference voltage and equals V_o of the PT-controlled buck converter. Assume that there are μ_H high-power pulses and μ_L low-power pulses in one system cycle. The oscillation frequency of the output voltage and inductor current f_M equals $1/T_M$, where pulse repetition cycle $T_M = (\mu_H + \mu_L)T$. Ignoring the influence of equivalent series resistance (ESR) of capacitor and variation of load resistance, in one system cycle of the traditional PT-controlled buck converter, the total changes of output voltage and inductor current are zero. Therefore, we have

$$\begin{cases} \mu_H \Delta v_{o,H} + \mu_L \Delta v_{o,L} = 0 \\ \mu_H \Delta i_{L,H} + \mu_L \Delta i_{L,L} = 0 \end{cases} \tag{3}$$

where $\Delta v_{o,H}$ and $\Delta v_{o,L}$ are the output voltage variations in one switching period with high-power pulse and low-power pulse, respectively, whereas $\Delta i_{L,H}$ and $\Delta i_{L,L}$ are variations of inductor current, respectively. D_H and D_L are the duty cycle of high- and low-power pulses, respectively. Hence, the ratio of the number of high-power pulses to low-power pulses in one system cycle is given by

$$\frac{\mu_H}{\mu_L} = \frac{|\Delta v_{o,L}|}{\Delta v_{o,H}} = \frac{|\Delta i_{L,L}|}{\Delta i_{L,H}}. \tag{4}$$

In a PT-controlled buck converter, we have

$$\frac{\mu_H}{\mu_L} = \frac{V_o - V_g D_L}{V_g D_H - V_o}. \tag{5}$$

From (5), the ratio of μ_H to μ_L is determined by the duty cycles of high- and low-power pulses, input voltage V_g, and output voltage V_o. There are two boundary voltages, namely the maximum and minimum output voltages, which are denoted as

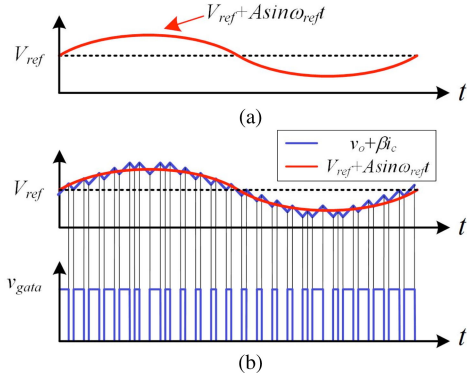

Fig. 3. Waveforms of reference voltage $V_{\rm ref}$, $\nu_o + \beta i_c$ and impulse waveform $v_{\rm gate}$.

$V_{\max}$ and $V_{\min}$, respectively, and $V_{\max} = D_H V_g$ and $V_{\min} = D_L V_g$. Hence, the output voltage V_o can only be regulated in the range $[V_{\min}, V_{\max}]$. When the PT-controlled buck converter operates in steady state, low-frequency oscillations of output voltage can be observed.

III. Proposed CC-PT/OFDM Method for Buck Converter

A. Communication Strategy Based on the CC-PT/OFDM Method

A CC-PT/OFDM-based PSST method is proposed in this study to mitigate low-frequency oscillations of the PT-controlled power converter and increase data transmission speed. The CC-PT method is adopted when W is ON, which can greatly suppress low-frequency oscillations by directing capacitor current into the voltage feedback loop.

The output duty cycle of the CC-PT control is determined by

$$D = \begin{cases} D_H, \beta i_c + v_o \le V_{\rm ref} + A\sin\omega_{\rm ref} t \\ D_L, \beta i_c + v_o \ge V_{\rm ref} + A\sin\omega_{\rm ref} t \end{cases} \tag{6}$$

where β is sampling gain of capacitor current, and the boundary condition for selecting pulse signals is given by

$$f = \beta i_c + v_o - V_{\rm ref} - A\sin\omega_{\rm ref} t. \tag{7}$$

Note that the information of inductor current ripple can also be reflected by capacitor current. When the transmitted signal using OFDM is added on the reference voltage, we have the converging law $\beta i_c + v_o = V_{\rm ref} + A\sin\omega_{\rm ref} t$. As shown in Fig. 3, the sinusoidal signal $A\sin\omega_{\rm ref} t$ is added to the reference voltage, and the superposition is consistent with the converging law by combining different high and low pulses. Equation (7) can now be rewritten as

$$f = \beta C \frac{dv_o}{dt} + v_o(t) - V_{\rm ref} - A\sin\omega_{\rm ref} t = 0. \tag{8}$$

Output voltage v_o is solved by

$$v_o(t) = V_{\rm ref} + C_1 e^{\frac{1}{\beta C} t} + \frac{A}{\sqrt{(\beta C \omega_{\rm ref})^2 + 1}} \sin(\omega_{\rm ref} t - \varphi). \tag{9}$$

Assuming the initial output voltage $v_o(0) = V_g$, we have

$$C_1 = V_g - V_{\text{ref}} - \frac{A\sin\varphi}{\sqrt{(\beta C\omega_{\text{ref}})^2 + 1}} = V_g - V_{\text{ref}} - \frac{A\beta C\omega_{\text{ref}}}{(\beta C\omega_{\text{ref}})^2 + 1}, \varphi = \arctan(\beta C\omega_{\text{ref}}). \tag{10}$$

When the overall system operates in steady state, output voltage v_o has the same frequency component as the sinusoidal signal added to reference voltage. With regards to multicarrier modulation technology, OFDM is employed here, which can eliminate the crosstalk between signals and overcome the frequency selective fading effect caused by a narrow signal bandwidth, low-frequency band, as well as unavoidable interferences.

Assume there are *N* subchannels in an OFDM system, and the subcarrier of each subchannel is

$$x_k(t) = A_k \cos(2\pi f_k t + \varphi_k) k = 0, 1, 2, \cdots, N-1 \tag{11}$$

where A_k is the subcarrier amplitude of the *k*th channel, f_k is the subcarrier frequency, and φ_k is its initial phase. Then, the composite signal generated by adding *N* subcarriers can be expressed as

$$s(t) = \sum_{k=0}^{N-1} x_k(t) = \sum_{k=0}^{N-1} A_k \cos(2\pi f_k t + \varphi_k). \tag{12}$$

Since any two subcarriers' signals are orthogonal, to demodulate *N* subcarriers from the receiver side, we have

$$\int_0^{T_b} \cos(2\pi f_i t + \varphi_i)\cos(2\pi f_j t + \varphi_j) dt = 0 \tag{13}$$

where T_b is one symbol duration time. Thus, the subcarrier meets the condition of

$$f_k = \frac{k}{2T_b} k = 0, 1, 2, \cdots, N-1. \tag{14}$$

The frequency interval of any two subcarriers satisfies

$$\Delta f = \frac{1}{T_b}. \tag{15}$$

If there are *N* subcarriers in the OFDM strategy, and each channel adopts *M*-ary modulation, the occupied frequency bandwidth is

$$B_{\text{OFDM}} = \frac{N+1}{T_b}. \tag{16}$$

The frequency band utilization rate is

$$\eta_{\text{OFDM}} = \frac{N\log_2 M}{T_b} \cdot \frac{1}{B_{\text{OFDM}}} = \frac{N}{N+1}\log_2 M. \tag{17}$$

As a carrier is used for *M*-ary data transmission, to ensure the same transmission rate, the duration of each code is shortened to be T_b/N, and the occupied bandwidth is $2N/T_b$. The frequency band utilization rate is

$$\eta_M = \frac{N\log_2 M}{T_b} \cdot \frac{T_b}{2N} = \frac{1}{2}\log_2 M. \tag{18}$$

Compared with single-carrier transmission, OFDM transmission strategy can double the frequency band utilization rate.

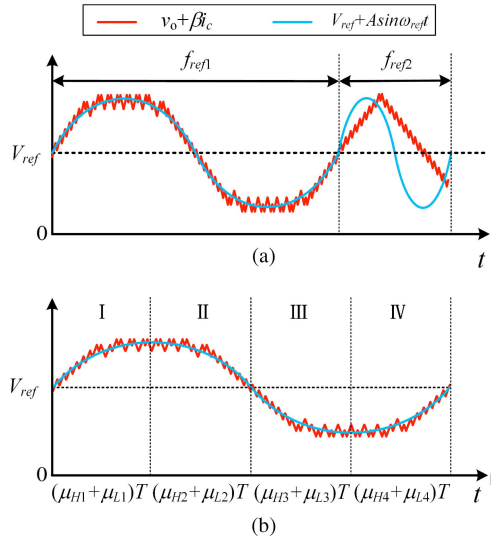

Fig. 4. Waveforms of the reference voltage with carrier $V_{ref} + A\sin\omega_{ref}t$ and feedback signal $v_o + \beta i_c$. (a) $v_o + \beta i_c$ incapable of tracking $V_{ref} + A\sin\omega_{ref}t$; (b) $v_o + \beta i_c$ capable of tracking $V_{ref} + A\sin\omega_{ref}t$.

B. Peak-to-Peak Output Voltage and Inductor Current

Both the capacitor current feedback gain β and the average frequency of the subcarriers f_{ref} can affect the performance of data transmission. The reference voltage with carriers $V_{\text{ref}} + A\sin\omega_{\text{ref}}t$ and signal $v_o + \beta i_c$ is shown in Fig. 4. The variation of the superimposed signal during one switching cycle is given by

$$\Delta(\beta i_c + v_o) = \beta\Delta(i_L - i_o) + \Delta v_o = \beta(\Delta i_L - I) + \left(1 - \frac{\beta}{R_{\text{eq}}}\right)\Delta v_o = \beta\left(\frac{T}{L}V_g D - \frac{T}{L}V_o - \frac{V_{Cn}^2}{Rv_o}\right) + \left(1 - \frac{\beta}{R_{\text{eq}}}\right)\Delta v_o. \tag{19}$$

The change of output voltage during one duty cycle is expressed as

$$\begin{aligned}\Delta v_o(nT) &= \frac{1}{C}\int_{nT}^{(n+1)T} i_c(t)dt = \frac{1}{C}\int_{nT}^{(n+1)T} \times \left[i_L(t) - \frac{V_o}{R_{\text{eq}}} - I\right]dt \\ &\approx \frac{1}{C}\left[DT\left[i_L(nT) + \frac{DT(V_g - V_o)}{2L}\right] + (1-D)T\left[i_L(nT) + \frac{DT(V_g - V_o)}{L} - \frac{V_o}{2L}(1-D)T\right]\right] \\ &\quad - \frac{V_o T}{CR_{\text{eq}}} - \frac{{V_{Cn}}^2 T}{CRV_o} \\ &= \frac{Ti_L(nT)}{C} + \frac{DT^2(V_g - V_o)(2-D) - V_o(1-D)^2T^2}{2LC} \\ &\quad - \frac{V_o T}{CR_{\text{eq}}} - \frac{{V_{Cn}}^2 T}{CRV_o}.\end{aligned} \tag{20}$$

Taking the average value of inductor current for approximation, we have

$$i_L(nT) = \frac{V_o}{R_{\text{eq}}} + I. \tag{21}$$

As shown in Fig. 4(b), when the converter operates in intervals I and IV, the total increment of the superimposed signal during a quarter of T_{ref} is approximately the amplitude of the sinusoidal carriers. As the intrinsic safety is also dependent on the peak-to-peak output voltage and inductor current, to account for the worst-case scenario, the maximum amplitude of carriers is defined as A_m. This is described by

$$\begin{cases} (\mu_{H1} + \mu_{L1})\, T = \frac{T_{\text{ref}}}{4} \\ \mu_{H1}\Delta\left(\beta i_c + v_o, D_H\right) + \mu_{L1}\Delta\left(\beta i_c + v_o, D_L\right) = A_m \end{cases} \tag{22.a}$$

$$\begin{cases} (\mu_{H4} + \mu_{L4})\, T = \frac{T_{\text{ref}}}{4} \\ \mu_{H4}\Delta\left(\beta i_c + v_o, D_H\right) + \mu_{L4}\Delta\left(\beta i_c + v_o, D_L\right) = A_m \end{cases}. \tag{22.b}$$

When the converter operates in intervals II and III, the total increments of the superimposed signal inside a quarter of T_{ref} approximately equals the negative amplitude of the sinusoidal carriers, which is expressed as

$$\begin{cases} (\mu_{H2} + \mu_{L2})\, T = \frac{T_{\text{ref}}}{4} \\ \mu_{H2}\Delta\left(\beta i_c + v_o, D_H\right) + \mu_{L2}\Delta\left(\beta i_c + v_o, D_L\right) = -A_m \end{cases} \tag{23.a}$$

$$\begin{cases} (\mu_{H3} + \mu_{L3})\, T = \frac{T_{\text{ref}}}{4} \\ \mu_{H3}\Delta\left(\beta i_c + v_o, D_H\right) + \mu_{L3}\Delta\left(\beta i_c + v_o, D_L\right) = -A_m \end{cases}. \tag{23.b}$$

From (22) to (23), within one period of the carrier signal, we have

$$\begin{cases} \mu_H = \mu_{H1} + \mu_{H2} + \mu_{H3} + \mu_{H4} \\ \mu_L = \mu_{L1} + \mu_{L2} + \mu_{L3} + \mu_{L4} \end{cases}. \tag{24}$$

Combining (22)–(24), the number of high- and low-power pulses in each period is given by

$$\mu_{H1} = \mu_{H4} = \frac{A_m - \Delta\left(\beta i_c + v_o, D_L\right)\frac{T_{\text{ref}}}{4T}}{\Delta\left(\beta i_c + v_o, D_H\right) - \Delta\left(\beta i_c + v_o, D_L\right)} \tag{25.a}$$

$$\mu_{L1} = \mu_{L4} = -\frac{A_m - \Delta\left(\beta i_c + v_o, D_H\right)\frac{T_{\text{ref}}}{4T}}{\Delta\left(\beta i_c + v_o, D_H\right) - \Delta\left(\beta i_c + v_o, D_L\right)}. \tag{25.b}$$

Defining f_{ref} as the average carrier frequency and f_s as the switching frequency, combining (19)–(21), (25-a), and (25-b), the peak-to-peak voltage of the output V_{pp} can be calculated by

$$\begin{aligned} V_{\text{pp}} &= \left|2(\mu_{H1}\Delta v_o(nT, D_H) + \mu_{L1}\Delta v_o(nT, D_L))\right| \\ &= \frac{R_{\text{eq}}}{\delta}\left[\beta V_o(1 - D_H - D_L) + \beta V_g D_H D_L \right. \\ &\quad \left. + \left(\beta L f_s \frac{V_{Cn}^2}{RV_o} + 4A_m L f_{\text{ref}}\right)(2 - D_H - D_L)\right] \end{aligned} \tag{26}$$

where

$$\delta = 2Lf_{\text{ref}}[(R_{\text{eq}} - \beta)(2 - D_H - D_L) + 2\beta C R_{\text{eq}} f_s].$$

The peak-to-peak current of the inductor, denoted as $i_{L\text{-pp}}$, is estimated by

$$\begin{aligned} i_{L-\text{pp}} &= \left|2(\mu_{H1}\Delta i_L(nT, D_H) + \mu_{L1}\Delta i_L(nT, D_L))\right| \\ &= \left|\frac{\frac{2\beta {f_s}^2 C V_{Cn}^2 L R_{\text{eq}}}{\delta R V_o} + \frac{8A_m C L R_{\text{eq}} f_s f_{\text{ref}} - (R_{\text{eq}} - \beta)V_o(1 - D_H - D_L) - (R_{\text{eq}} - \beta)V_g D_H D_L}{\delta}}{}\right|. \end{aligned} \tag{27}$$

Hence, the peak inductor current I_{LP} is given by

$$\begin{aligned} I_{LP} &= I_o + I + \frac{1}{2} i_{L-\text{pp}} = \frac{V_o}{R_{\text{eq}}} + \frac{V_{Cn}^2}{RV_o} + \frac{\beta {f_s}^2 C V_{Cn}^2 L R_{\text{eq}}}{\delta R V_o} \\ &\quad + \left|\frac{8A_m C L R_{\text{eq}} f_s f_{\text{ref}} - (R_{\text{eq}} - \beta)V_o(1 - D_H - D_L) - (R_{\text{eq}} - \beta)V_g D_H D_L}{2\delta}\right|. \end{aligned} \tag{28}$$

Equation (28) also shows that I_{LP} can be reduced by increasing L.

C. System Iteration Model

To facilitate numerical calculations, the system iteration model is built. As per (2), the change of output voltage and capacitor current in one switching cycle can be written by

$$\begin{cases} \Delta v_o(nT) = \frac{T^2}{2LC}\left[\left(V_g D(2 - D) - v_o(nT)\right)\right] \\ \qquad\qquad + \frac{T}{C} i_c(nT) \\ \Delta i_c(nT) = \frac{T}{L}\left(\frac{T}{2R_{\text{eq}}C} - 1\right) v_o(nT) - \frac{T}{R_{\text{eq}}C} i_c(nT) \\ \qquad\qquad + \frac{T}{L} V_g D\left[1 - \frac{T}{2R_{\text{eq}}C}(2 - D)\right] \end{cases} \tag{29}$$

The mapping function of the CC-PT-controlled buck converter with the output voltage and capacitor current as state variables can be obtained by

$$X_{n+1} = \begin{cases} MX_n + B^H, CX_n \le V_{\text{ref}} + A_m \sin \omega_{\text{ref}} nT \\ MX_n + B^L, CX_n > V_{\text{ref}} + A_m \sin \omega_{\text{ref}} nT \end{cases} \tag{30}$$

where

$$X_{n+1} = \begin{bmatrix} v_o[(n+1)T] \\ i_c[(n+1)T] \end{bmatrix}, X_n = \begin{bmatrix} v_o(nT) \\ i_c(nT) \end{bmatrix}$$

$$M = \begin{bmatrix} 1 - \frac{T^2}{2LC}\frac{T}{C} \\ \frac{T^2}{2R_{\text{eq}}LC} - \frac{T}{L}1 - \frac{T}{R_{\text{eq}}C} \end{bmatrix}$$

$$B^H = \begin{bmatrix} \frac{T^2}{2LC} V_g D_H (2 - D_H) \\ \frac{T}{L} V_g D_H - \frac{T^2}{2R_{\text{eq}}LC} V_g D_H (2 - D_H) \end{bmatrix}$$

$$B^L = \begin{bmatrix} \frac{T^2}{2LC} V_g D_L (2 - D_L) \\ \frac{T}{L} V_g D_L - \frac{T^2}{2R_{\text{eq}}LC} V_g D_L (2 - D_L) \end{bmatrix}$$

$$C = [1\beta]^T.$$

Hence, the output voltage and capacitor current are regulated as the reference voltage V_{ref} and feedback gain β change. The standard deviation is introduced here to represent the proximity

between the superimposed signal and the reference voltage as

$$\sigma(\beta, f_{\text{ref}}) = \sqrt{\frac{1}{J}\sum_{i=1}^{J}\left[v_{oi} + \beta i_{ci} - V_{\text{ref}} - A_m \sin \omega_{\text{ref}} iT\right]^2} \tag{31}$$

where J represents the number of sampling points for calculation when the system operates at steady state. The standard deviation reflects the distance between the superimposed signal and the reference voltage.

IV. Parameter Design for Intrinsically Safe CC-PT/OFDM-Based Buck Converter

It is essential to select correct parameters to build an intrinsically safe buck converter, considering output voltage ripple, inductor discharging, and output short-circuiting. Parameters design method for the traditional buck converter is studied in [28]. Since the peak-to-peak output voltage and inductor current ripples vary, as the CC-PT control method and OFDM communication operate in the buck converter, parameters for intrinsically safe buck converter also change. Based on the peak-to-peak output voltage V_{pp}, peak-to-peak inductor current $i_{L\text{-pp}}$, and peak inductor current I_{LP} shown in (26), (27), and (28), parameters can be redesigned for the intrinsically safe CC-PT/OFDM-based buck converter with the method introduced below.

A. Minimum Capacitance Based on Voltage Ripple

According to the circuit topology, reducing capacitance leads to a larger ripple amplitude. However, the ripple must be restricted to guarantee the output power quality.

To achieve safety and high power quality of the output voltage for OFDM communication, assuming $V_{\text{pp}} < mV_{\text{o}}$, based on (26), the minimum capacitance $C_{\min}$ must satisfy

$$V_{\text{pp}}(C_{\min}) = mV_o. \tag{32}$$

The minimum capacitance is then derived by

$$\begin{aligned} C_{\min} = {} & \frac{1}{4m\beta RLf_s f_{\text{ref}}}[\beta R V_g V_o D_H D_L + \beta R {V_o}^2 \\ & \times (1 - D_H - D_L) \\ & + (\beta V_{Cn}^2 L f_s + 4RV_o A_m L f_{\text{ref}})(2 - D_H - D_L)] \\ & - \frac{(R_{\text{eq}} - \beta)(2 - D_H - D_L)}{2\beta f_s R_{\text{eq}}}. \end{aligned} \tag{33}$$

B. Maximum Inductance

A large inductor stores more energy and can cause large arc discharging current when the inductor is accidentally disconnected, which damages the converters operating in harsh environments. With the CC-PT/OFDM method in the buck converter, peak inductor current I_{LP} changes with the relation in (28). So, the maximum inductance for a buck converter with the CC-PT/OFDM method should be redesigned to guarantee the arc discharging safety upon inductor disconnection.

The inductor disconnection arc discharging (IDAD) testing circuit with a standard spark apparatus is shown in Fig. 5(a),

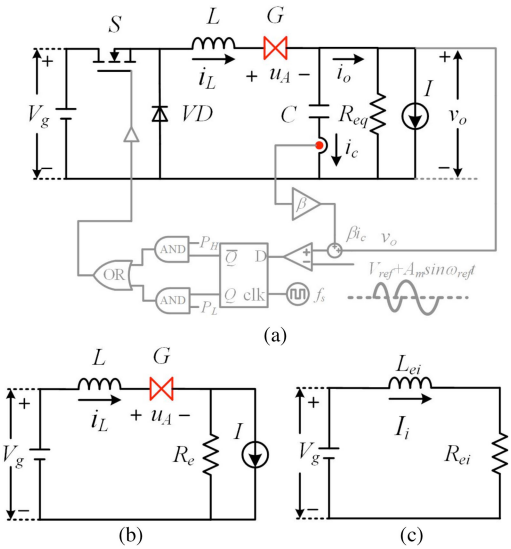

Fig. 5. IDAD test: (a) Buck converter with disconnection of the inductor; (b) equivalent circuit of safety spark; (c) equivalent inductive arc circuit of the switching converter.

where G represents the safety spark apparatus, and u_A is the IDAD voltage. The equivalent spark experimental circuit is shown in Fig. 5(b), and the equivalent arc inductive circuit is shown in Fig. 5(c).

Based on the single linear attenuation model, the discharging inductor current of the buck converter with the CC-PT/OFDM method is expressed as

$$i_L(t) = \left(\frac{V_g}{R_e} + I\right)\left(1 - \frac{t}{T_L}\right). \tag{34}$$

The IDAD voltage is expressed as

$$u_A(t) = \frac{V_g}{T_L}\left(t + \frac{L}{R_e}\right) \tag{35}$$

where T_L is the discharging time, and R_e is the dynamic equivalent resistance. The IDAD energy W_{eq} in the simplified equivalent inductive circuit is given by

$$\begin{aligned} W_{\text{eq}} &= \int_0^{T_L} u_A(t) i(t) dt \\ &= \frac{1}{6} V_g I_{\text{eq}} T_L + \frac{1}{2} L I_{\text{eq}}^2 + \frac{1}{6}\frac{V_{Cn}^2 V_g T_L}{RV_o} + \frac{V_{Cn}^2 V_g L}{2R_e RV_o} \end{aligned} \tag{36}$$

where I_{eq} is the equivalent current.

Assume that the output voltage decreases linearly within the IDAD interval [29]. The output voltage $v_{\text{o}}(t)$ and its varied quantity Δv during the discharging time T_L are given by

$$\begin{aligned} v_o(t) &= V_o\left(1 - \frac{t}{R_{\text{eq}} C}\right) \\ \Delta v &= v_o(0) - v_o(T_L) = \frac{T_L}{R_{\text{eq}} C} V_o. \end{aligned} \tag{37}$$

In the equivalent arc inductive circuit of the switching converter, according to the single linear attenuation model, during the IDAD period, the IDAD voltage of the safety spark apparatus

is derived by

$$u_A(t) = V_g + \frac{LI_{LP}}{T_L} - R_e(I_{LP} - I) + \frac{R_e(I_{LP} - I)}{T_L}t \quad (38)$$

where $R_e = \Delta v/\Delta I = \Delta v/I_{LP}$. When the inductor is disconnected, the arc voltage surges from 0 to $V_{A,\min}$, which satisfies

$$u_A(0) = V_{A,\min} \quad (39)$$

where $V_{A,\min}$ is the minimal arc voltage. Ignoring the equivalent current source and by combining (37)–(39), T_L and Δv can be derived by (40) and (41) shown at the bottom of this page.

During the IDAD period, the arc energy of the buck converter W_A is expressed as

$$W_A = \frac{1}{2}V_g I_{LP} T_L + \frac{1}{2}LI_{LP}^2 + \frac{1}{2}C[V_o^2 - (V_o - \Delta v)^2] - \frac{T_L(3V_o^2 - 3V_o\Delta v + \Delta v^2)}{3R_{\text{eq}}}. \quad (42)$$

Let $W_A = W_{\text{eq}}$. The equivalent-current I_{eq} is given by

$$I_{\text{eq}} = \sqrt{\frac{6W_A V_{A,\min}}{L(V_g + 3V_{A,\min})}}. \quad (43)$$

With the single linear attenuation model, the arc energy W_{ei} of the simplified equivalent inductive circuit is given by

$$W_{ei} = \frac{1}{6}V_g I_{LP} T_{Lei} + \frac{1}{2}L_{ei}I_{LP}^2 \quad (44)$$

where $T_{Lei} = LI_{LP}/V_{A,\min}$. Because the arc energy equals the IDAD energy, i.e., (44) equals (36), the equivalent inductance L_{ei} can be expressed by

$$L_{ei} = L\frac{I_{eq}^2}{I_{LP}^2} + \frac{V_{Cn}^2 V_g T_L}{3RV_o I_{LP}^2} + \frac{V_{Cn}^2 V_g L}{RR_e V_o I_{LP}^2}. \quad (45)$$

We can see that when $I = 0$, $L_{ei} = LI_{eq}{}^2/I_{LP}{}^2$. Searching the inductance L_{eB} on the experimental IDAD test curve, the maximum inductance is realized, when $L_{ei} = L_{eB}$. The equivalent inductance L_{ei} satisfies

$$L_{ei} < L_{eB}. \quad (46)$$

C. Maximum Capacitance

A large capacitor stores a large amount of energy and can potentially lead to a fierce spark at the terminal when the output is short-circuited. Because the capacitor current in the CC-PT/OFDM-based buck converter is different from that in the conventional converter, the amounts of the short-circuit sparking energy also differ. The capacitance should be limited to ensure that the accidental spark cannot damage the buck converter with the CC-PT/OFDM method.

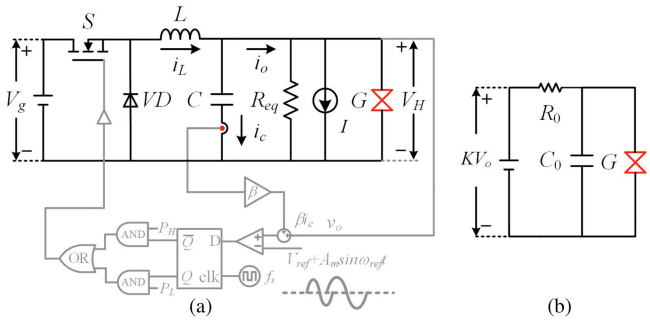

Fig. 6. Output short-circuit sparking test: (a) circuit of the sparking test; (b) simplified equivalent capacitive circuit of sparking test.

Fig. 6(a) depicts the schematic of the sparking test when the output is short-circuited, whereas Fig. 6(b) displays the simplified equivalent capacitive circuit for the sparking test. When the output is short-circuited, the arc energy mainly comes from the source—W_S, the inductor—W_L, the current source—W_I, and the capacitor—W_C. Meanwhile, the resistor consumes part of energy—W_R. Assume the duration from when short-circuiting happens to when the switch completely turns OFF is Δt, and the maximum arc energy released when output is short-circuited is calculated as

$$\begin{aligned} W_{\text{arc}} &= W_S + W_L + W_C + W_I - W_R \\ &= V_g I_{LP}\Delta t + \tfrac{V_g^2}{L}\Delta t^2 + \tfrac{1}{2}CV_o{}^2 + V_o I\Delta t - \tfrac{V_H^2 T_C}{R_{\text{eq}}} \\ &= \{\tfrac{8A_m CLR_{\text{eq}} f_s f_{\text{ref}} - (R_{\text{eq}}-\beta)[V_o(1-D_H-D_L) - (R_{\text{eq}}-\beta)V_g D_H D_L]}{2\delta} \\ &+ \tfrac{V_o}{R_{\text{eq}}} + \tfrac{V_{Cn}^2}{RV_o} + \tfrac{\beta f_s{}^2 CILR_{\text{eq}}}{\delta}\}V_g\Delta t + \tfrac{V_g^2}{L}\Delta t^2 \\ &+ \tfrac{1}{2}CV_o{}^2 + \tfrac{V_{Cn}^2\Delta t}{R} - \tfrac{V_H^2 T_C}{R_{\text{eq}}}. \end{aligned} \quad (47)$$

For instance, suppose $\Delta t = 2\ \mu$s, the average discharging voltage $V_H = 8$ V, and the spark discharging period $T_C = 200\ \mu$s. Based on energy conservation, the equivalent capacitance C_e while short-circuited is

$$C_e = \frac{2W_{\text{arc}}}{V_o^2}. \quad (48)$$

According to the simplified equivalent capacitive circuit, considering a safety margin K (from 1.5 to 2), for a converter with the output voltage V_o, the ignition capacitance C_B is searched on the experimental minimal ignition voltage curve when the ignition voltage is KV_o, so the equivalent capacitance should satisfy

$$C_e < C_B. \quad (49)$$

$$T_L = \frac{R_{\text{eq}}C(V_g - V_{A,\min}) + \sqrt{R_{\text{eq}}{}^2C^2(V_{A,\min} - V_g)^2 + 4V_o LI_{LP}R_{\text{eq}}C}}{2V_o} \quad (40)$$

$$\Delta v = \frac{V_g - V_{A,\min}}{2} + \frac{\sqrt{R_{\text{eq}}{}^2C^2(V_{A,\min} - V_g)^2 + 4V_o LI_{LP}R_{\text{eq}}C}}{2R_{\text{eq}}C}. \quad (41)$$

TABLE I
SYSTEM PARAMETERS

Symbol	Quantity	Values
V_g	input voltage	24V
R_{eq}	load resistance	50Ω
f_s	switching frequency	200kHz
V_{ref}	reference voltage	12V
f_{ref}	average frequency of subcarriers	1250 Hz
β	feedback coefficient	0.3
D_H	duty cycle of high pulses	0.7
D_L	duty cycle of low pulses	0.3
N	the number of subcarriers	4
A	amplitude of sinusoidal signals	0.1V

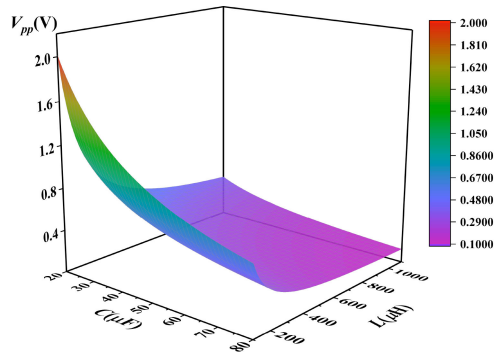

Fig. 7. 3-D plot of the output peak-to-peak voltage $V_{\rm pp}$ against *L*–*C* changes.

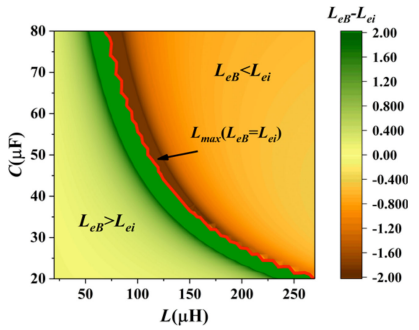

Fig. 8. Contour map showing the distance of L_{eB} and L_{ei} and the maximal inductance curve.

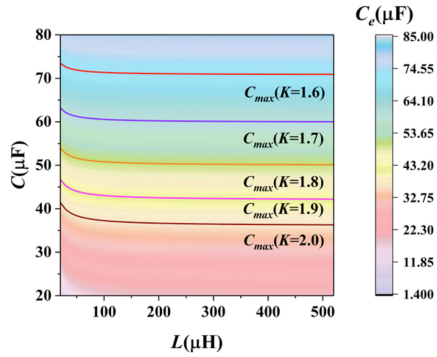

Fig. 9. Contour map of the equivalent capacitance and the maximum capacitance curve.

V. SIMULATION AND EXPERIMENTAL VERIFICATION

A. Simulations

Based on the MATLAB/Simulink, PLECS, and PSIM platforms for designing the intrinsically safe region, system parameters are chosen and listed in Table I, to verify the feasibility of OFDM communication in the buck converter.

With the parameters listed in Table I, based on (26), the 3-D mapping of peak-to-peak output voltage $V_{\rm pp}$ is drawn in Fig. 7. It proves that $V_{\rm pp}$ decreases as the capacitance increases. Overall, the mathematical model can be used to estimate the state variables of the CC-PT-controlled buck converter with OFDM communication.

System parameters are listed in Table I, where A_m is selected as *NA* (0.4 V). The variation of output voltages corresponding to high and low duty cycles can be calculated, which are $0.166i_L(nT)$-0.0097(V) and $0.166i_L(nT)$-0.0393(V), respectively. Due to the variation of inductor current $i_L(nT)$, the output voltage during one duty cycle is difficult to predict. The average value of inductor current is 0.6 A, and the output voltage variations are 0.9873 and 0.9606 V, respectively. The peak-to-peak output voltage is 1.0518 V, which is close to the simulation result shown in the *L*–*C* area. The peak-to-peak inductor current $i_{L\text{-pp}}$ is calculated to be 0.4092 A, and hence, the peak inductor current I_{LP} is 1.0092 A. The standard deviation between $v_{\rm o} + \beta i_c$ and the carriers is 0.12.

The minimum arcing voltage $V_{A,\min}$ is usually selected as 10 V. As an example, when $D_H = 0.7$, $D_L = 0.3$, $\beta = 0.3$, $A = 0.1$ V, $V_g = 24$ V, $V_{\rm o} = 12$ V, $R_{\rm eq} = 50\ \Omega$, $f_s = 200$ kHz, and $f_{\rm ref} = 1250$ Hz, the contour map showing the distance of $L_{\rm eB}$ and $L_{\rm ei}$ is depicted in Fig. 8. The critical condition of inductor disconnection discharging safety criterion is that $L_{\rm eB}$ equals $L_{\rm ei}$, or $L_{\rm eB}$-$L_{\rm ei} = 0$, so the contour line $L_{\rm eB}$-$L_{\rm ei}$ being 0 is also the curve of the maximal inductance $L_{\max}$, which is marked with the red line. The system satisfies the IDAD safety when L_{ei} is smaller than L_{eB}. So, the green area below the $L_{\max}$ curve indicates the IDAD safe *L*–*C* parameter space while the system is dangerous when the inductance and capacitance locate in the yellow area.

By searching the chart of minimal ignition voltage, the contour map of the equivalent capacitance C_e and the maximum capacitance curve $C_{\max}$ under various safety margins is drawn on the *L*–*C* plane. In Fig. 9, the intrinsically safe region shrinks as the safety margin *K* increases, and the maximum capacitance curve $C_{\max}$ becomes flat when the inductance is large.

Combining the aforementioned analyses and criteria, the intrinsically safe region is finally determined by finding the intersection surrounded by three critical curves in (33), (46), (49), and horizontal axis. When margins are set as $m = 0.5$ and $K = 1.7$, by drawing three critical curves, the intrinsically safe region is thus determined, as shown in Fig. 10. As long as the inductance and capacitance locate in the intrinsically safe region, the buck converter with the CC-PT/OFDM methods can operate with intrinsic safety. In the experiments, the intrinsically safe capacitance *C* and inductance *L* are selected as 30 μF and 150 μH, respectively.

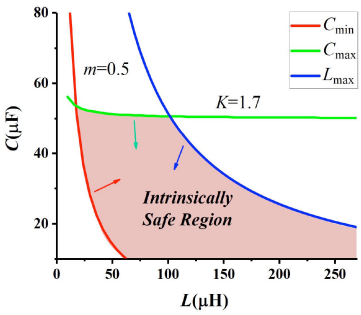

Fig. 10. Intrinsically safe region of buck converter with the CC-PT/OFDM method.

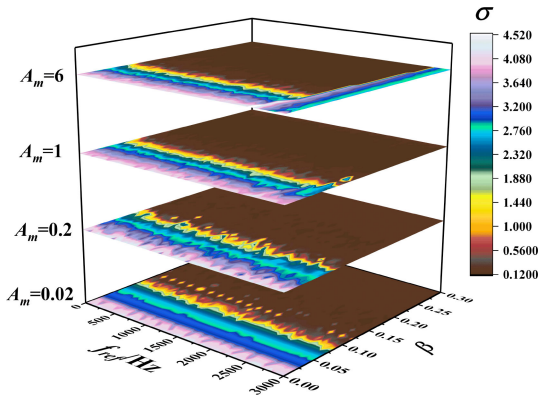

Fig. 11. Standard deviation of superposed signal $v_o + \beta i_c$.

According to the system iteration model in (30), when $C = 30\ \mu$F and $L = 150\ \mu$H, the standard deviation σ of the superimposed signal $v_{\rm o} + \beta i_c$ under different carrier amplitudes, frequencies, and feedback parameters is drawn in Fig. 11. It is obvious that a smaller feedback parameter β leads to a higher standard deviation, and a large amplitude of reference voltage leads to a larger region with higher standard deviation, which means a narrow parameters ($f_{\rm ref}$ and β) space. This infers that the superimposed signal follows $V_{\rm ref} + A_m \sin\omega_{\rm ref} t$ closely when the feedback parameter is selected as 0.3, the amplitude of the reference voltage is 0.1 V, and frequencies of the reference voltage are chosen from 0.5 to 2 kHz. In the envelope tracking and visible light communication fields, a higher carrier frequency can be chosen to transmit more information in the same time interval [30]. The maximum subcarrier frequency is selected as 2 kHz here to guarantee high tracking accuracy between $v_{\rm o} + \beta i_c$ and carriers. Note that, a higher frequency band around switching frequency could be occupied or interfered with by harmonics from other power converters, so a relatively low carrier frequency is employed to fully use the frequency band of signal channel and also can avoid the interference from other power converters. Moreover, the signal transmission rate by using a subcarrier of 2 kHz is sufficient in the application of state monitoring and operation alert in harsh environments.

When the capacitor current feedback parameter is $\beta = 0.3$, and the frequency of the subcarriers equals f_a (0.5 kHz), f_b (1 kHz), f_c (1.5 kHz), and f_d (2 kHz), respectively. The output waveforms

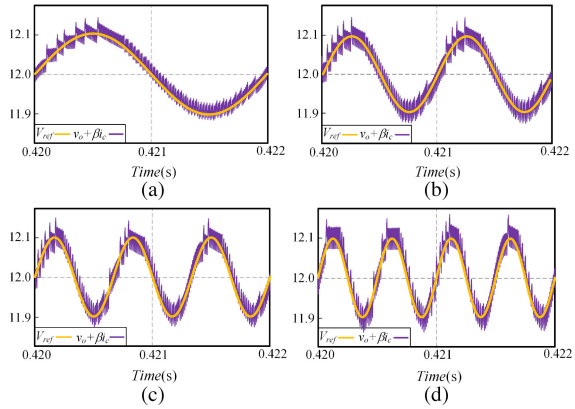

Fig. 12. Waveforms of the reference voltage and the superimposed $v_o + \beta i_c$ in PSIM simulations. (a) $f_a = 500$ Hz. (b) $f_b = 1000$ Hz. (c) $f_c = 1500$ Hz. (d) $f_d = 2000$ Hz.

TABLE II
CARRIER SIGNALS TRUTH TABLE

Carrier signals				Base-band signal
f_a	f_b	f_c	f_d	
0	0	0	0	0000
0	0	0	1	0001
0	0	1	0	0010
0	0	1	1	0011
0	1	0	0	0100
0	1	0	1	0101
0	1	1	0	0110
0	1	1	1	0111
1	0	0	0	1000
1	0	0	1	1001
1	0	1	0	1010
1	0	1	1	1011
1	1	0	0	1100
1	1	0	1	1101
1	1	1	0	1110
1	1	1	1	1111

of $v_{\rm o} + \beta i_c$ are shown in Fig. 12. These reference voltages with four different frequencies constitute the carrier combinations for OFDM communication.

To ensure no interference among the carrier signals, one symbol duration time T_b is set to 0.05 s, and the carrier signal truth table is reported in Table II, where code "0" indicates no signal modulation, whereas code "1" means the presence of code modulation.

For instance, four bits in each frame are transmitted in parallel by the subcarriers generated by four modulators, respectively. The output voltage waveform is shown in Fig. 13.

Through the OFDM parallel transmission strategy, which doubles the transmission rate, two carrier signals of different frequencies can appear in one code interval. Since the two carriers are orthogonal to each other, they can be identified separately.

B. Experimental Validation

Experimental parameters are listed in Table I, and the carrier modulation is chosen in sequence through the truth table in

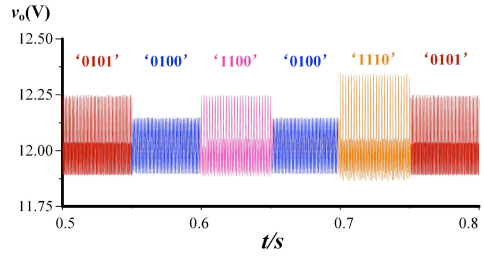

Fig. 13. Waveform of output voltage in PLECS simulations.

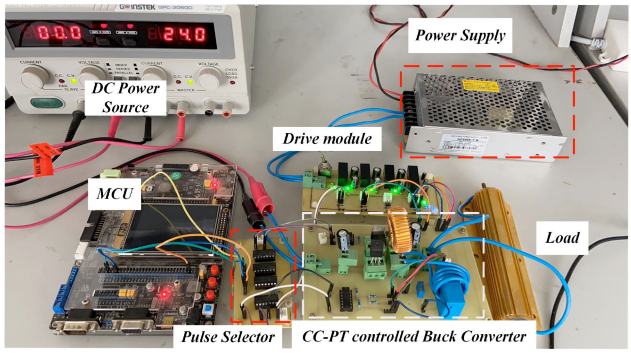

Fig. 14. Experimental platform.

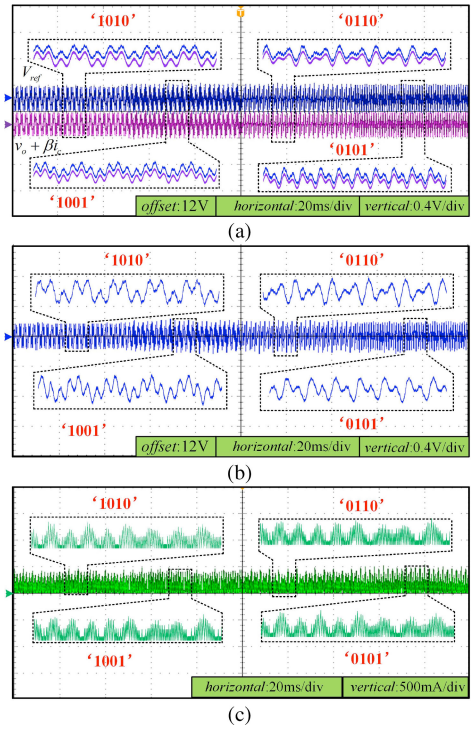

Fig. 15. Experimental waveforms of the CC-PT/OFDM modulation: (a) signal $v_o + \beta i_c$ and reference voltage; (b) output voltage; (c) inductor current.

Table II. The photograph of the experimental platform with components marked is shown in Fig. 14. Microcontroller unit STM32F407 is used to generate high- and low-power pulses for OFDM modulation.

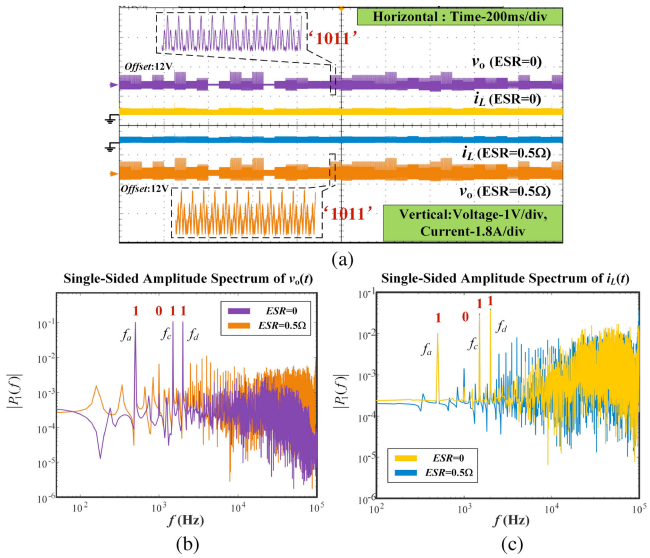

Fig. 16. Influences of capacitor ESR: (a) waveforms of output voltage and inductor current with and without ESR (0.5 Ω); (b) amplitude spectrum of $v_o(t)$ when transmitting "1011"; (c) amplitude spectrum of $i_L(t)$ when transmitting "1011."

Fig. 15(a) depicts the waveform of the reference voltage and the superimposed signal $v_o + \beta i_c$. The superimposed signal is consistent with the convergence law-$v_o + \beta i_c \rightarrow V_{\text{ref}} + A_m \sin\omega_{\text{ref}} t$. Fig. 15(b) shows the waveform of the output voltage, which agrees with the waveform obtained in the simulation. The frequencies of the ripples contained in the output voltage are consistent with the transmission codes, which are shown in the carrier signal truth table. Moreover, the maximum output voltage is approximately 12.4 V. The inductor current waveform is shown in Fig. 15(c), and its maximum value is 0.6 A. Because the experimental parameters are selected in the intrinsically safe region and are tested in the standard deviation maps, the communication in the CC-PT-controlled buck converter with the OFDM strategy is carried out with intrinsic safety.

Considering the influence of capacitor ESR, waveforms of output voltage as well as inductor current with and without ESR are shown in Fig. 16(a) for comparison. It can be seen that, in comparison with testing results of zero ESR, ESR of 0.5 Ω increases the amplitude of the output voltage, and could hence jeopardize the converter's intrinsic safety. However, since the value of ESR is quite small, its effect on the intrinsic safety region caused by capacitor ESR is negligible. Take signal sequence "1011" as an example. The amplitude spectra of output voltage $v_o(t)$ and inductor current $i_L(t)$ are drawn in Fig. 16(b) and (c), respectively. Although ESR can result in high-frequency harmonics, the carrier frequencies f_a, f_c, and f_d for transmitting signal "1011" can still be detected for demodulation. Hence, although capacitor ESR could lead to power quality deterioration, the proposed PSST strategy functions well as it can demodulate signals from high-frequency noise of both output voltage and inductor current.

Load variation is also tested to validate the effectiveness of the proposed strategy. Take the signal sequence "1110" as example.

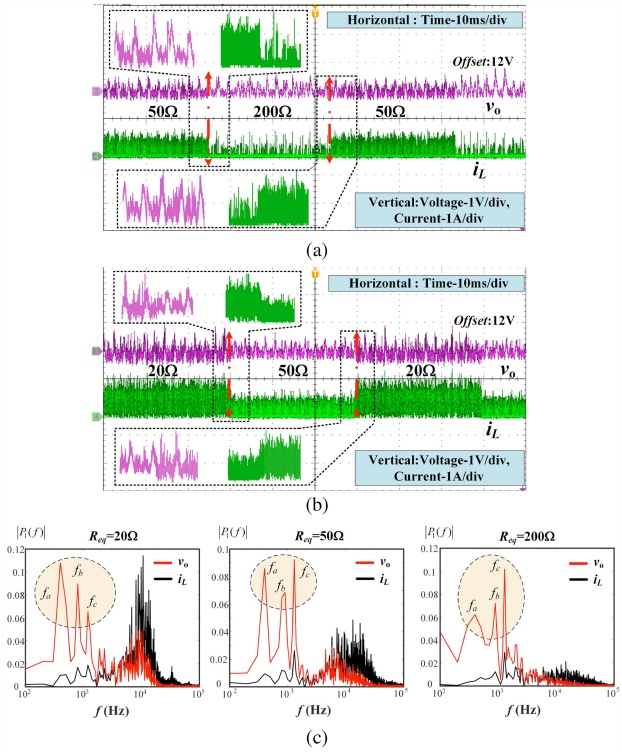

Fig. 17. Load variation test. (a) Load variation between 50 and 200 Ω. (b) Load variation between 50 and 20 Ω. (c) Amplitude spectrums of $v_o(t)$ and $i_L(t)$ with different load when transmitting "1110."

The testing results are shown in Fig. 17(a) and (b) as the load increases to 200 Ω and decreases to 20 Ω, respectively. With regards to signal modulation, amplitude spectrums of output voltage and inductor current under three different loads are drawn in Fig. 17(c). The oscillation amplitude of output voltage can be increased by reducing the load, whereas the amplitude of inductor current can be reduced by increasing the load. The dominant carrier frequency components sampled from the dc bus is used for signal demodulation. As circled in Fig. 17(c), frequencies f_a, f_b, and f_c can be evidently detected together with f_d, which is used for representing sequence "1110." The amplitude of high-frequency harmonics is in fact reduced as load increases. However, the amplitude of carrier frequency becomes less distinctive for the testing case with a 200-Ω load, as well as shown by the inductor current frequency spectrum. Since the transmitted signal is demodulated by ripples sampled from the dc bus, the proposed strategy can function well under a wide range of load owing to its quick response speed and distinct frequency components of output voltage ripples.

Fig. 18(a) depicts waveforms of arc voltage, current, and power in the inductor disconnection test. The disconnected arc energy $W_A = 0.000875$ J. Based on (43) and (45), assuming $V_{A,\min} = 10$ V, the equivalent current $I_{\text{eq}} = 2.53$ A, and the equivalent inductance $L_{ei} = 1.926$ mH, which is smaller than the critical inductance L_{eB} (2.2 mH). So, the arc energy cannot ignite the gas in the inductor disconnection test.

Fig. 18(b) shows the arc voltage, current, and its power waveforms in the output short-circuit test. The sparking process

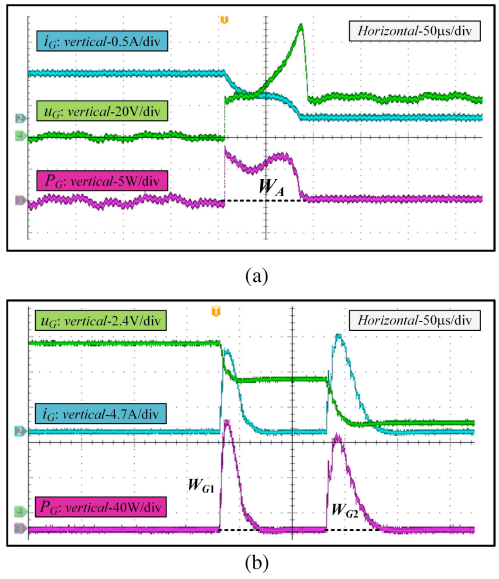

Fig. 18. Arc voltage, current, and power waveforms for (a) inductor disconnection test and (b) output short-circuit test.

is divided into three stages, including the first discharging period, voltage maintenance, and the second discharging period. The arc energy W_{arc} is released within two discharging stages, which is represented by two power bulges W_{G1} and W_{G2}. Arc energy W_{arc} can be estimated by $W_{G1} + W_{G2}$ (0.0051 J). Based on (49), the equivalent capacitance C_e is calculated as 17.7 μF, which is below the critical capacitance C_B (36 μF) when the margin K is selected as 2.0. This proves that this system is intrinsically safe in the output short-circuit test.

Overall, both the arc energy in the inductor disconnection test and the output short-circuit test are smaller than that of the critical conditions, and the intrinsic safety of the CC-PT-controlled buck converter with OFDM-PSST is ensured.

VI. Conclusion

In this article, a novel PSST strategy based on the OFDM is proposed for the CC-PT-controlled buck converter with intrinsic safety. The approach of the CC-PT/OFDM modulation is illustrated, with detailed mathematical models of the CC-PT-controlled buck converter with OFDM communication established. Considering the intrinsic safety requirements on the output voltage ripples, the inductor disconnection discharging, and the output short-circuit spark test, critical conditions are analyzed by mathematical modeling and then drawn on the *L–C* plane. Through simulations and experiments, selected typical system parameters, which are chosen in the intrinsically safe region and evaluated by standard deviations, are proved to be feasible for the OFDM communication in the CC-PT-controlled buck converter. With the advantages of simple structure, high response speed, and intrinsic safety, the proposed CC-PT/OFDM method doubles the communication speed of its conventional counterpart, realizes the PSST in dc–dc converters, and promotes safety and coordination of switching power supply, bringing great industrial application value.

The main limitation of the work lies in that the signal transmission speed of PSST is still low, which hence cannot be applied in scenarios needing high-speed communication. Also, the signal transmission distance is affected by the bus line impedance.

REFERENCES

[1] M. Q. Liu, K. Yang, and N. Zhao, "Intelligent signal classification in industrial distributed wireless sensor networks based Industrial Internet of Things," *IEEE Trans. Ind. Informat.*, vol. 17, no. 7, pp. 4946–4956, Jul. 2021.

[2] Y. D. Li, L. Zhang, and Z. Lv, "Detecting anomalies in intelligent vehicle charging and station power supply systems with multi-head attention models," *IEEE Trans. Intell. Transp. Syst.*, vol. 22, no. 1, pp. 555–564, Jan. 2021.

[3] Z. Y. Zhang, J. Dyer, and X. Y. Wu, "Online junction temperature monitoring using intelligent gate drive for SiC power devices," *IEEE Trans. Power Electron.*, vol. 34, no. 8, pp. 7922–7932, Aug. 2019.

[4] S. L. Liu, H. Wu, and Y. X. Zhang, "The analysis and design of high-power intrinsic safe forward converter based on Power-i technology," in *Proc. 5th Int. Conf. Elect. Eng.*, Jan. 2019, Art. no. 012015.

[5] Y. Li, S. L. Liu, and H. Gao, "A simplified output voltage ripple calculation method of intrinsically safe buck converter with LC low pass filter," in *Proc. 14th IEEE Conf. Ind. Electron. Appl.*, Jun. 2019, pp. 1536–1539.

[6] Y. Chen, B. Zhang, F. Xie, D. Qiu, and Y. Chen, "The time-invariant polynomial model of fixed-frequency PWM DC-DC converter applying normalized coordinate transformation," *IEEE Trans. Power Electron.*, vol. 36, no. 11, pp. 13200–13214, Nov. 2021.

[7] S. Valadkhani and M. Mirsalim, "Variable output voltage switching rectifier for cathodic protection applications with DC–DC variable frequency and duty-cycle full-bridge converter," *IEEE Trans. Power Electron.*, vol. 36, no. 12, pp. 13589–13602, Dec. 2021.

[8] J. Zhao, H. H. C. Iu, and T. Fernando, "A design of single-switch two-stage DC-DC converters with PWM and PFM for off-grid solar power system," *Chin. J. Elect. Eng.*, vol. 3, no. 3, pp. 44–51, Dec. 2017.

[9] H. Luo, J. Xu, D. He, and J. Sha, "Pulse train control strategy for CCM boost PFC converter with improved dynamic response and unity power factor," *IEEE Trans. Ind. Electron.*, vol. 67, no. 12, pp. 10377–10387, Dec. 2020.

[10] X. Zan *et al.*, "A new control strategy for SR generation system based on modified PT control," *IEEE Access*, vol. 7, pp. 179720–179733, 2019.

[11] D. S. Yu, Y. S. Geng, and H. H. C. Iu, "Pulse phase shift based low-frequency oscillation suppression for PT controlled CCM buck converter," *IEEE Trans. Circuits Syst. II, Exp. Briefs*, vol. 65, no. 10, pp. 1465–1469, Oct. 2018.

[12] H. Luo, J. P. Xu, and D. Y. He, "Pulse train control strategy for CCM boost PFC converter with improved dynamic response and unity power factor," *IEEE Trans. Ind. Electron.*, vol. 67, no. 12, pp. 10377–10387, Dec. 2020.

[13] Y. S. Geng, D. S. Yu, Z. L. Xia, and R. D. Xu, "Parallel-connected buck converters controlled by capacitor current feedback based PT with current-sharing ability," *IET Power Electron.*, vol. 11, no. 15, pp. 2481–2489, Dec. 2018.

[14] J. Sha, Y. M. Chen, and J. P. Xu, "A peak-capacitor-current pulse-train-controlled buck converter with fast transient response and a wide load range," *IEEE Trans. Ind. Electron.*, vol. 63, no. 3, pp. 1528–1538, Mar. 2016.

[15] D. S. Yu, L. Wang, F. Xie, and R. D. Xu, "Novel sliding valley current mode pulse train control for switching DC-DC converter," *Int. J. Electron.*, vol. 106, no. 2, pp. 250–266, Feb. 2019.

[16] M. N. Soares, Y. Mollet, and M. Kinnaert, "Multiphysical time-and frequency-domain fault detection and isolation technique for power-electronic converters in DFIG wind turbines," *IEEE Trans. Power Electron.*, vol. 36, no. 4, pp. 3793–3802, Apr. 2021.

[17] M. W. Ahmad, N. B. Y. Gorla, and H. Malik, "A fault diagnosis and postfault reconfiguration scheme for interleaved boost converter in PV-based system," *IEEE Trans. Power Electron.*, vol. 36, no. 4, pp. 3769–3780, Apr. 2021.

[18] D. Miller, G. Mirzaeva, and C. D. Townsend, "The use of power line communication in standalone microgrids," *IEEE Trans. Ind. Appl.*, vol. 57, no. 3, pp. 3029–3037, May/Jun. 2021.

[19] X. N. He, R. C. Wang, and J. D. Wu, "Nature of power electronics and integration of power conversion with communication for talkative power," *Nature Commun.*, vol. 11, May 2020, Art. no. 2479. [Online]. Available: https://doi.org/10.1038/s41467-020-16262-0

[20] J. D. Wu, J. Du, and Z. Y. Lin, "Power conversion and signal transmission integration method based on dual modulation of DC-DC converters," *IEEE Trans. Ind. Electron.*, vol. 62, no. 2, pp. 1291–1300, Feb. 2015.

[21] J. H. Chen, J. D. Wu, and R. C. Wang, "Coded PWM based switching ripple communication applied in visible light communication," *IEEE Trans. Power Electron.*, vol. 36, no. 8, pp. 9659–9667, Aug. 2021.

[22] J. Du, J. Wu, R. Wang, Z. Lin, and X. He, "DC power-line communication based on power/signal dual modulation in phase shift full-bridge converters," *IEEE Trans. Power Electron.*, vol. 32, no. 1, pp. 693–702, Jan. 2017.

[23] D. S. Yu *et al.*, "A novel power and signal composite modulation approach to power line data communication for SRM in distributed power grids," *IEEE Trans. Power Electron.*, vol. 36, no. 9, pp. 10436–10446, Sep. 2021.

[24] A. M. Jaradat, J. M. Hamamreh, and H. Arsian, "Modulation options for OFDM-based waveforms: Classification, comparison, and future directions," *IEEE Access*, vol. 7, pp. 17263–17278, 2019, doi: 10.1109/ACCESS.2019.2895958.

[25] Y. X. Li, M. Zhang, and W. G. Zhu, "Performance evaluation for medium voltage MIMO-OFDM power line communication system," *China Commun.*, vol. 17, no. 1, pp. 151–162, Jan. 2020.

[26] Y. Wang, R. Yang, B. Zhang, and W. Hu, "Smale horseshoes and symbolic dynamics in the buck–boost DC–DC converter," *IEEE Trans. Ind. Electron.*, vol. 65, no. 1, pp. 800–809, Jan. 2018.

[27] Y. X. Zhao, M. G. Li, and Q. Wang, "Optimal design method for inner-intrinsically safe buck-boost converters based on ignition capability," *Math. Problems Eng.*, vol. 2021, Feb. 2021, Art. no. 6678566. [Online]. Available: http://doi.org/10.1155/2021/6678566

[28] S. L. Liu, H. Wu, and C. Y. Wang, "Inner intrinsically safe criterion and design considerations of buck converters based on equivalent inductance," *Elect. Power Compon. Syst.*, vol. 47, no. 3, pp. 248–260, Feb. 2019.

[29] G. H. Zhou, Y. Li, M. R. Leng, Z. Gong, and G. D. Xu, "Stabilizing effect of load converter in cascaded system considering ripple interaction," *IEEE Trans. Circuit Syst. II, Exp. Briefs*, vol. 68, no. 1, pp. 296–300, Jan. 2021.

[30] J. Rodríguez, J. R. García-Meré, D. G. Aller, and J. Sebastián, "Pulsewidth modulated three-level buck converter based on stacking switch-cells for high power envelope tracking applications," *IEEE Trans. Power Electron.*, vol. 37, no. 5, pp. 5786–5800, May 2022.

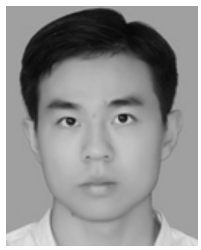

Yang Leng received the B.S. degree in electrical engineering and automation from the School of Electrical Engineering and its Automation, Henan Polytechnic University, Jiaozuo, China, in 2018, and the M.S. degree in electrical engineering from the School of Electrical Engineering, China University of Mining and Technology, Xuzhou, China, in 2021.

He has authored or coauthored many research papers. His research interests include nonlinear dynamics, memristive systems, power and signal synchronous transmission, power electronics, and intrinsically safe converters.

Mr. Leng was a recipient of one Best Paper Award from international conference. He serves as a Reviewer for *Circuit World*, *International Journal of Bifurcation and Chaos*, and IEEE OPEN JOURNAL OF POWER ELECTRONICS.

Dongsheng Yu (Member, IEEE) received the B.Eng. in electrical engineering and automation and the Ph.D. degree in electrical engineering from the School of Information and Electrical Engineering, China University of Mining and Technology, Xuzhou, China, in 2005 and 2011, respectively.

From 2009 to 2010, he was a Visiting Student with The University of Western Australia, Perth, WA, Australia. In 2014, he was an Endeavour Research Fellow with The University of Western Australia. He is currently a Full Professor with the School of Electrical Engineering, China University of Mining and Technology. He has authored or coauthored two books and more than 80 papers in his research interests, which include power electronics, power line communication, fault monitoring and diagnosis, nonlinear dynamics, and memristive systems.

Kunfeng Han received the B.S. degree in electrical engineering and its automation from the Shandong University of Science and Technology, Qingdao, China, in 2018. He is currently working toward the M.S. degree in electrical engineering with the China University of Mining and Technology, Xuzhou, China.

His current research interests include pulse train control technique, intrinsically safe converters, and communication technique applied in dc–dc converters.

Samson Shenglong Yu (Member, IEEE) received the master's degree in electrical and electronic engineering and the Ph.D. degree in electrical engineering from The University of Western Australia (UWA), Perth, WA, Australia, in 2014 and 2017, respectively.

From 2011 to 2012, he was an Electronics Design and Testing Engineer. From 2017 to 2019, he was a Postdoctoral Research Fellow with UWA. Since August 2019, he has been an Assistant Professor (Lecturer) with Deakin University, Melbourne, VIC, Australia. Since 2015, he has authored or coauthored more than 80 journal articles, book chapters, and technical reports in highly renowned international publication fora. He has been working with international scholars on a wide range of industrial and research projects in battery technology, electrical faults, technology for future readiness in microgrids, etc. His research interests include systems engineering, systems dynamics, power systems, renewable energy integration, applied electronics and control, and nonlinear systems.

Yihua Hu (Senior Member, IEEE) received the B.S. degree in electrical engineering and the Ph.D. degree in power electronics and drives from the China University of Mining and Technology, Xuzhou, China, in 2003 and 2011, respectively.

Between 2011 and 2013, he was with the College of Electrical Engineering, Zhejiang University, Hangzhou, China, as a Postdoctoral Fellow. Between 2013 and 2015, he was a Research Associate with the Power Electronics and Motor Drive Group, University of Strathclyde, Glasgow, U.K. Between 2016 and 2019, he was a Lecturer with the Department of Electrical Engineering and Electronics, University of Liverpool, Liverpool, U.K. He is currently a Reader with the Electronics Engineering Department, University of York, York, U.K. He has authored or coauthored more than 120 papers in IEEE Transactions journals. His research interests include renewable generation, power electronics converters and control, electric vehicle, more electric ship/aircraft, smart energy system, and nondestructive test technology.

Dr. Hu is the Associate Editor for the IEEE TRANSACTIONS ON INDUSTRIAL ELECTRONICS, *IET Renewable Power Generation*, *IET Intelligent Transport Systems*, and *Power Electronics and Drives*. He is a Fellow of the Institution of Engineering and Technology. He was awarded the Royal Society Industry Fellowship.